Surface & Coatings Technology 512 (2025) 132366

Contents lists available at ScienceDirect

Surface & Coatings Technology

journal homepage: www.elsevier.com/locate/surfcoat

Protective thermal spray coatings for TES applications in CSP plants☆

Lorena Betancor-Cazorla, Adela Svobodova-Sedlackova, Genís Clavé, Camila Barreneche, Sergi Dosta*

Departament de Ciència de Materials i Química Física, Universitat de Barcelona, C/Martí i Franqués 1, 08028 Barcelona, Spain

ARTICLE INFO

Keywords:
Thermal spray
Corrosion
Thermal energy storage (TES)
Concentrating solar power (CSP)
Coatings
Molten salt
Nanofluids

ABSTRACT

Corrosion caused by using molten salts in thermal storage systems in Concentrated Solar Power (CSP) plants is a major problem in this field. To eliminate this problem, the use of nanofluids and the application of Inconel-625 coatings by thermal spray techniques (High Velocity Oxygen Fuel - HVOF and Cold Gas Spray - CGS) are proposed. This study focuses on evaluating the effectiveness of these coatings, deposited on AISI 316 stainless in mitigating nanofluid-induced corrosion in CSP plant Thermal Energy Storage (TES) systems. For this purpose, a total immersion test in $NaNO_3$ with silica nanoparticles was carried out in a furnace at 450 °C under air atmosphere for 30 days (720 h) and 90 days (2160 h). The test was also performed on SS316L and Inconel-625 bulk substrate samples for better comparison. Evaluation of corrosion behaviour relied on measuring the reduction in cross-sectional thickness of the test samples. Furthermore, detailed characterization was performed using Laser Scattering (LS), Scanning Electron Microscopy (SEM), and Field Emission Scanning Electron Microscopy (FESEM). The coating surface was also studied by X-Ray Diffraction (XRD), and the molten salt-based nanofluids were studied by Inductively Coupled Plasma (ICP). The results obtained revealed notably minimal corrosion rates per year for both deposition methods, after 3 months of testing. This demonstrates the effectiveness of both HVOF and CGS Inconel-625 coatings as a reliable solution to decrease the level of corrosion in TES units. However, future studies should be conducted over longer periods and with operating conditions closely replicating working conditions.

1. Introduction

In the last decade, the energy system has experienced a great transformation to reduce its environmental impact. In 2023, global renewable capacity increased by almost 50 % to nearly 510 gigawatts (GW), the fastest-growing rate in the past two decades. Photovoltaic and wind energy, besides hydroelectricity, predominate in the current renewable energy market, accounting for 95 % of global renewable expansion [1].

Despite the high efforts to incorporate renewable energies into our energy system share and cost reductions, certain limitations remain, mainly dominated by the security of supply due to the intermittence of renewable energies. The decarbonization of the network and the subsequent substitution of traditional resources necessitate the development of an energy grid that optimizes cost and efficiency between generation and storage. At this point, concentrating solar power plants (CSP) with thermal storage systems (TES) come into play. They address the low energy storage capacity and the high cost of batteries for wind and PV technology [2,3]. At the end of 2022, CSP installed capacity increased by 200 MW, reaching a total of 6.3 GW [4], where all the new facilities incorporate a thermal energy storage system. Thanks to thermal storage systems, CSP plants have the potential to produce 24/7 baseload and/or peak electric power. These power plants can also operate overnight until the storage ends by avoiding the combined-cycle-gas backup. Between 2010 and 2021, due to technological improvements, the levelized cost of energy (LCOE) of CSP plants fell by 68 %, motivated by the addition of TES systems, improving plants' dispatchability while decreasing LCOE [5]. Despite the benefits, the total deployment of this technology is limited, among other factors, by the high LCOE, not yet competitive in the market [6,7].

Nowadays, the most commercially utilized configuration in CSP with TES is the two-tank with molten salts, concretely with the so-called solar salts, which are a mixture of sodium and potassium nitrates (60 % wt. $NaNO_3$–40 % wt. KNO_3) [8]. The dual tank configuration consists of a

☆ This article is part of a Special issue entitled: '11RIPT' published in Surface & Coatings Technology.

* Corresponding author.
E-mail address: sdosta@ub.edu (S. Dosta).

https://doi.org/10.1016/j.surfcoat.2025.132366
Received 28 October 2024; Received in revised form 22 April 2025; Accepted 2 June 2025
Available online 3 June 2025
0257-8972/© 2025 The Authors. Published by Elsevier B.V. This is an open access article under the CC BY-NC-ND license (http://creativecommons.org/licenses/by-nc-nd/4.0/).

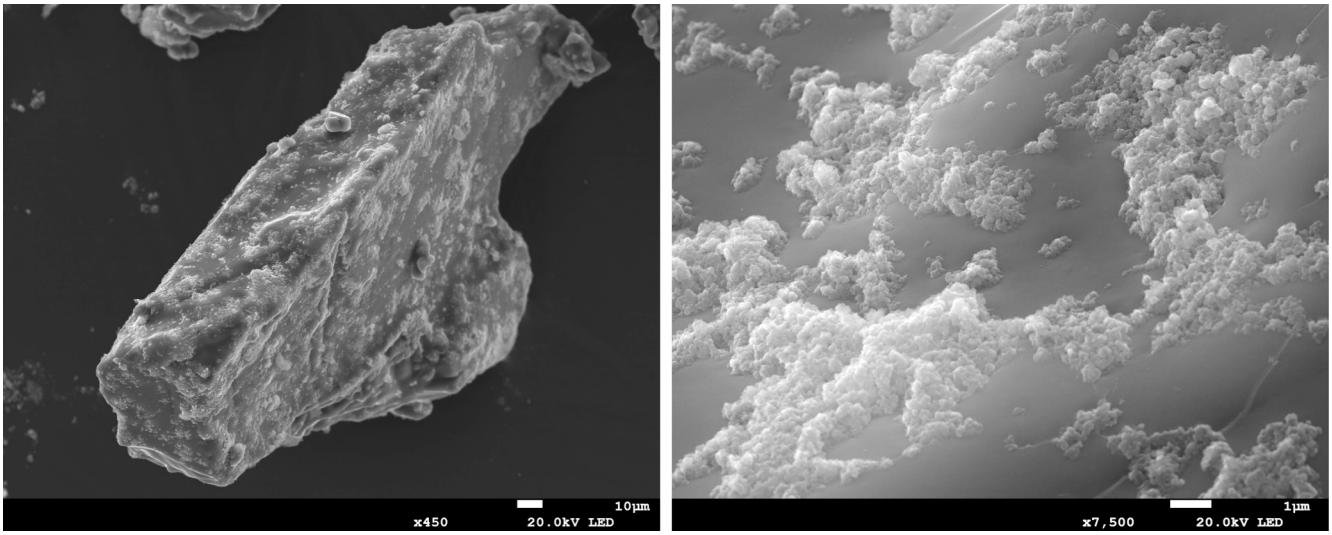

Fig. 1. Molten salt-based nanofluids FESEM micrographs (500×-1500×, 20 kV).

cold tank operating at around 290 °C and a hot tank reaching temperatures of approximately 565 °C (depending on the specific technology.) These tanks are designed to maintain the sensible heat of molten salt until it is needed for power generation. This technology achieves annual efficiency of up to 99 % [9,10]. Despite the good properties and technological maturity, molten salt-based systems are limited by relatively low heat capacity and thermal stability, especially corrosion issues. Molten salts are corrosive and even more prominent with the increase in temperature, causing corrosion to the metals in contact. Therefore, the selection of the material for the construction of the TES tanks is a critical point; the materials need to have high corrosion resistance, preventing leaks, structural damage, and low contamination of the molten salts due to the corrosion products [11,12]. Consequently, the global performance in terms of dispatchability and capacity factor of CSP is partly motivated by the improvement of the storage tanks [13,14].

One of the ways to improve it is to enhance the thermal properties of the storage medium. In this sense, a new kind of fluid has been studied in the past years, the so-called nanofluids [15]. Nanofluids are colloidal suspensions of low nanoparticle concentration in a fluid that exhibit unusually enhanced thermophysical properties like a specific heat capacity or thermal conductivity of >30 % in front of the base fluid [16,17]. Molten salt-based nanofluids, although their development is still under study [18], show great potential as a thermal storage medium. Over 250 publications from 2009 to the end of 2021 have been published about molten salt-based nanofluids, highlighting (1) the tendency of enhanced specific heat capacity of molten salts, indicating the feasibility to enhance the storage density of the system; higher heat capacity and storage temperatures result in a reduced tank volume requirements [19–21]. (2) Increased thermal stability; molten salts with higher thermal stability allow work at higher temperatures, enhancing the Brayton cycle and, therefore, its efficiency [22–24]. (3) Reduction of corrosion rates due to the incorporation of nanoparticles in the salt-wall interfaces, forming a protective layer to prevent metal corrosion [25–27].

This last finding is relevant because corrosion plays a relevant role in TES [28]. When designing the tank, the wall thickness must be determined based on the corrosion rate of the material in contact with the molten solar salts at each tank temperature, considering the entire 30-year lifecycle of the storage system. Nowadays, some of the most commercial metals used for the construction of the storage tank are carbon steel ASTM A516 Gr. 70 alloy (generally for the cold tank) and AISI A-347H, AISI 316 L, AISI 321, and AISI 304 alloys (generally for the hot tank) [28]. These materials cover two key points in the design of the TES tanks: good corrosion resistance and excellent mechanical properties that provide great structural strength and longevity [11]. Corrosion directly affects the materials used, the operating temperatures, the number of thermal cycles, and the type of molten salt employed. It also influences the tank's lifecycle, as higher corrosion causes structural failure, thus increasing maintenance costs [11,14,29]. Therefore, developing alloys or different ways to prevent corrosion in the tanks is essential and is another way to improve the storage tanks.

In this context, thermal spray coatings are a possible solution to minimize corrosion and damage to TES system materials. These can act as a protective layer to prevent direct contact between the molten salts and the equipment. Of the different thermal spray processes, high-velocity oxy-fuel (HVOF) and cold gas spray (CGS) deposition have been growing in recent decades due to their ability to improve the mechanical strength of materials, as well as their durability [30–33]. In addition to extending the service life of TES tanks, they also make it possible to create low-cost and environmentally friendly coatings [31,34,35]. In recent years, some research has been carried out using HVOF and CGS coatings to reduce corrosion effects caused by molten salts [36–39]. In general, coatings deposited by these techniques are durable, with good thermal stability, and perform well against corrosion at high temperatures. However, despite the good results in molten salts, almost no research is available regarding their behaviour with molten salt-based nanofluids.

Accordingly, to the actual paradigm, the main aim of this research is to evaluate the useful life cycle of the storage tank, preventing its premature structural damage motivated mainly by hot corrosion. To this end, this study combines two strategies: use of nanofluids as a thermal medium with 1%wt. of SiO_2 nanoparticles and the use of Inconel-625 HVOF and CGS coatings as a solution to reduce the corrosion of TES tanks in CSP plants. A corrosion test under static conditions is performed at 450 °C, during 30 and 90 days to evaluate the corrosion rate of the system. Therefore, the main objective of the study is to develop effective coatings to reduce corrosion, improving the efficiency and competitiveness of CSP.

2. Materials, methods, and experimental procedures

2.1. Molten salt-based nanofluids synthesis

The preparation of the molten salt-based nanofluids (Fig. 1) was performed following the same procedure as in previous studies [40]. Commercial sodium nitrate (Sigma Aldrich, 99.995 % purity) in powder or crystals (melting point: 308 °C) was used. The nanoparticles used were silica nanopowders (Sigma Aldrich, 99.5 % purity) with a particle

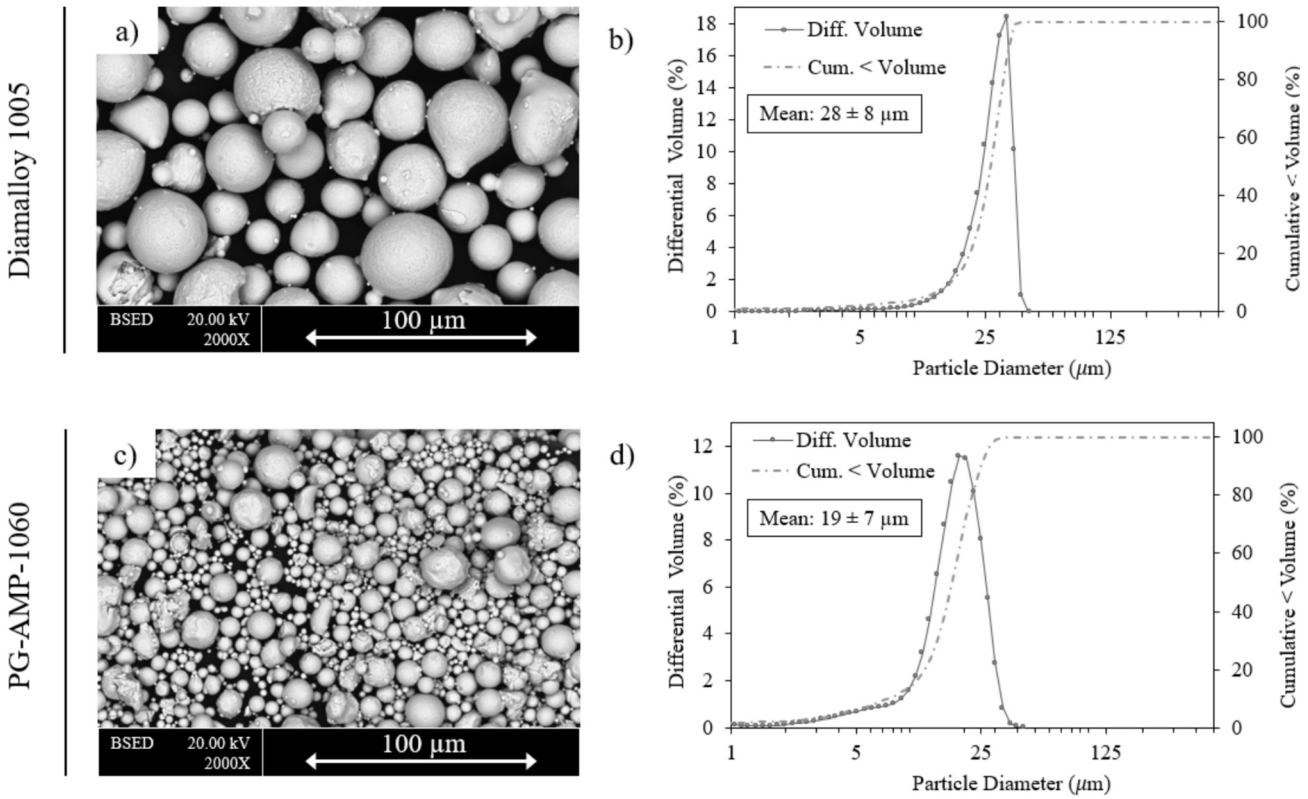

Fig. 2. Scanning electron image of the powders (2000×, 20 kV): a) Diamalloy 1005 and c) PG-AMP-1060, and particle size distribution in volume (%): b) Diamalloy 1005 and d) PG-AMP-1060.

Table 1
Inconel-625 powders chemical composition.

	Composition (wt%)						
Powder	Ni	Cr	Mo	Nb/Ta	Fe	Al	Si
Diamalloy 1005	65.3 ± 1.9	21.2 ± 0.3	8.9 ± 0.6	2.9 ± 0.3	1.2 ± 0.6	0.4 ± 0.1	0.3 ± 0.1
PG-AMP-1060	63.1 ± 0.6	22.4 ± 0.2	9.7 ± 0.6	3.8 ± 0.1	0.2 ± 0.1	0.4 ± 0.1	0.4 ± 0.1

size of 10–20 nm (BET) and a melting point >1600 °C. The preparation procedure used was the standard two-step method with dissolution [41]: (1) preparing 80 g of sample with 1 wt% SiO_2 and dissolve in 30 ml of distilled water (2) mix homogeneously with a sonicator (3) drying the mixture in a furnace at 105 °C until complete evaporation of the water and (4) grinding in an Agate mortar the recrystallized salt.

2.2. Corrosion test materials

AISI 316 L stainless steel substrates with Inconel-625 coatings were subjected to the corrosion test. Diamalloy 1005 powder (Fig. 2-a) was used for the HVOF samples, and PG-AMP-1060 powder (Fig. 2-c) for the CGS samples. The composition of the powders is shown in Table 1. Both powders have a spherical morphology, with a particle size of −37 + 18 µm for Diamalloy 1005 (Fig. 2-b) and − 27 + 8 µm for PG-AMP-1060 (Fig. 2-d).

Notice that due to its nature, Inconel 625 has better corrosion resistance than SS316L, which is the current material used to build TES tanks. However, when Inconel is sprayed as a coating, just a 200–300 µm-thick layer is obtained, and its application enhances the durability of the material in use.

2.3. Spray coating techniques

Before the coating layers were deposited, the samples were grit-blasted with Al_2O_3 to activate the surface, increase the roughness, and remove oxidation.

CGS samples were supplied by Titomic Europe B·V., a company based in the Netherlands. A PCS100 Japan Cold Spray machine from Plasma Giken Co., Ltd., was used. The process gas was N_2, with a flow rate of 700–900 l/min, and the operating conditions ranged from 900 °C to 1100 °C and 50 to 70 bars.

HVOF samples were produced at the Spanish company TMCOMAS. For the deposition of the coatings, the materials were sprayed with Inconel reference parameters (250–280 mm stand-off distance) with a Oerlikon DJH2700 gun using natural gas as fuel (300–350 l/min).

2.4. Experimental procedure corrosion test

Before performing the corrosion test, the samples were roughened to obtain a regular and uniform coating surface. The remaining sample sides were coated with a thermal paste (Nural 30, from Pattex). This ensured that the test was performed only on the side where the coating was deposited. A total immersion corrosion test procedure was followed in a furnace at 450 °C under air atmosphere for 30 days (720 h) and 90 days (2160 h). The 8 samples were placed in alumina crucibles and

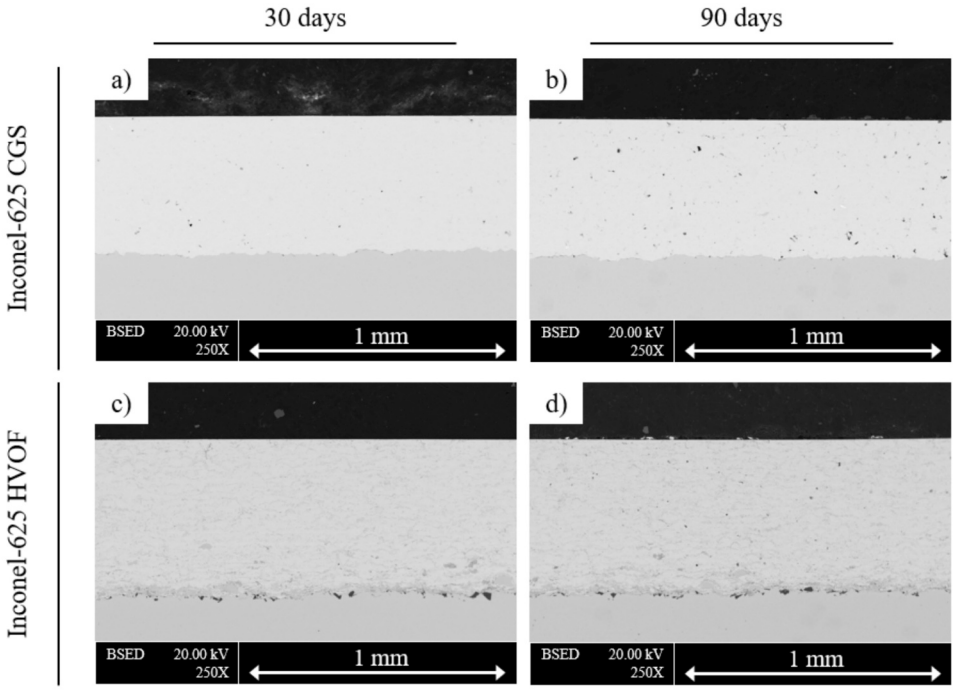

Fig. 3. SEM images of the cross-section of samples of a) Inconel-625 CGS after 30 days, b) Inconel-625 CGS after 90 days, c) Inconel-625 HVOF after 30 days, and d) Inconel-625 HVOF after 90 days.

covered by nanofluids. Two samples of CGS and two samples of HVOF were tested (one each for 30 and 90 days). For a better comparison, the test was also performed on SS316L substrate and Inconel-625 bulk for periods of 30 days and 90 days.

2.5. Characterization methods

2.5.1. Sample preparation

The ABRASIMENT 250 cutting machine with a 60A25 abrasive disc was used to perform the cross-section of the samples after the corrosion test was completed. To facilitate the manipulation of the specimens during roughing and polishing, the samples were pressed in hot resin on a REMET - IPA 30 EVOLUTION machine.

2.5.2. Corrosion rate calculation

The corrosion rate (μm/year) was calculated based on the reduction in coating thickness (Eq. 1). To evaluate this reduction, an average was calculated using the cross-section of the samples (before the test, 1-month test, 3-month test), taking measurements along the entire coating from SEM images. For the samples in which the reduction was unclear (HVOF, Inconel-625 bulk and SS316 L samples), an average of the oxide layers formed was calculated following the same procedure. Thus, the total sample thickness reduction was determined by eliminating the area covered by the oxide layer formed.

$$Corrosion\ rate\left(\frac{\mu m}{year}\right) = \frac{\Delta thickness\ (\mu m)}{time\ test\ (days)} \cdot \frac{365\ days}{1\ year} \quad (1)$$

Table 2
Coating thickness measurements of Inconel-625 deposited by CGS and HVOF techniques initially and after corrosion test at 450 °C during 30 and 90 days.

Sample	Coating thickness (μm)		
	Initial	30 days	90 days
Inconel-625 CGS	551 ± 8	553 ± 5	544 ± 14
Inconel-625 HVOF	607 ± 5	607 ± 9	608 ± 8

2.5.3. Characterization techniques

The particle size distribution (PSD) of the Inconel-625 powders was measured using a Beckman Coulter LS 13320, with acetone as fluid. The morphology of coatings and powders was initially analysed using a QUANTA 200 electron microscopy equipment with EDS, and the detailed cross-section mappings of samples and salt micrographs were obtained using a FESEM JEDL J-7100 microscope (GATAN MONO-CL4 cathodoluminescence spectrometer, EDS detector, backscattered electron detector).

The X-ray diffraction (XRD) test was performed with PANalytical X'Pert PRO MPD, Bragg-Brentano powder diffractometer with 240 mm radius. Six samples were tested: Diamalloy 1005 powder, PG-AMP-1060 powder, Inconel-625 HVOF, Inconel-625 CGS, Inconel-625 HVOF after 3 months of corrosion testing and Inconel-625 CGS after 3 months of corrosion testing. For the powder samples and Inconel-625 coatings, Fe-filtered Co $K\alpha$ radiation was used, with measurements taken in continuous scanning mode and 2θ range from 7° to 125° with a step size of 0.017° and a measurement time of 100 s per step. For Inconel-625 samples after 3 months of corrosion testing, Ni-filtered Cu $K\alpha$ radiation was used, with scan in the 2θ range from 4.5° to 100° with a step size of 0.026° and a measuring time of 100 s per step. To allow a better comparison of the results, the Cu signal was transformed to Co.

Inductively Coupled Plasma Atomic Emission Spectroscopy (ICP-AES) and Inductively Coupled Plasma Mass Spectrometry (ICP-MS) were performed to detect and identify the metal elements present in the samples' composition. Nanofluid-based salt samples (100 mg) were mixed with 1 ml of HNO_3 and 1 ml of HF, for 24 h in an oven at 90 °C. For the salt of the CGS sample, 0.5 ml of HF was added for 2 h at 90 °C because it still had residue. After that, 45 ml H_2O (high purity) were added to the mixture for 12 h at 90 °C. The samples were analysed in two steps; the first step involved using the ICP-AES technique, which was performed on PerkinElmer ELAN 6000 ICP mass spectrometer to analyse Si content. In the second step the ICP-MS was employed to analyse Cr, Mo and Ni-based on the detection limit of the technique, and an ICP-OES simultaneous Perkin Elmer Optima 3200R spectrometer was used to analyse these elements.

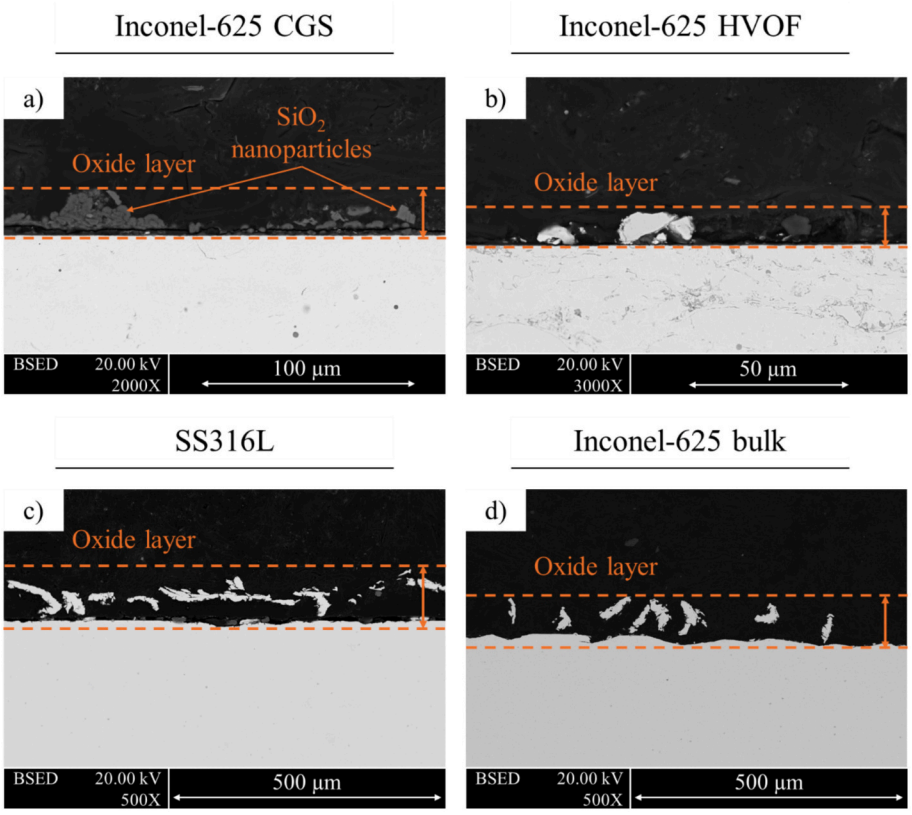

Fig. 4. SEM images of the samples surface after 3 months: a) Inconel-625 CGS, b) Inconel-625 HVOF, c) SS316L and d) Inconel-625 bulk.

3. Results and discussion

After immersion in sodium nitrate-based nanofluids for 30 and 90 days, the Inconel-625 samples deposited with HVOF and CGS remained almost unaffected by corrosion, as seen in Fig. 3. In addition, the coating thickness loss was evaluated to determine the corrosion progression

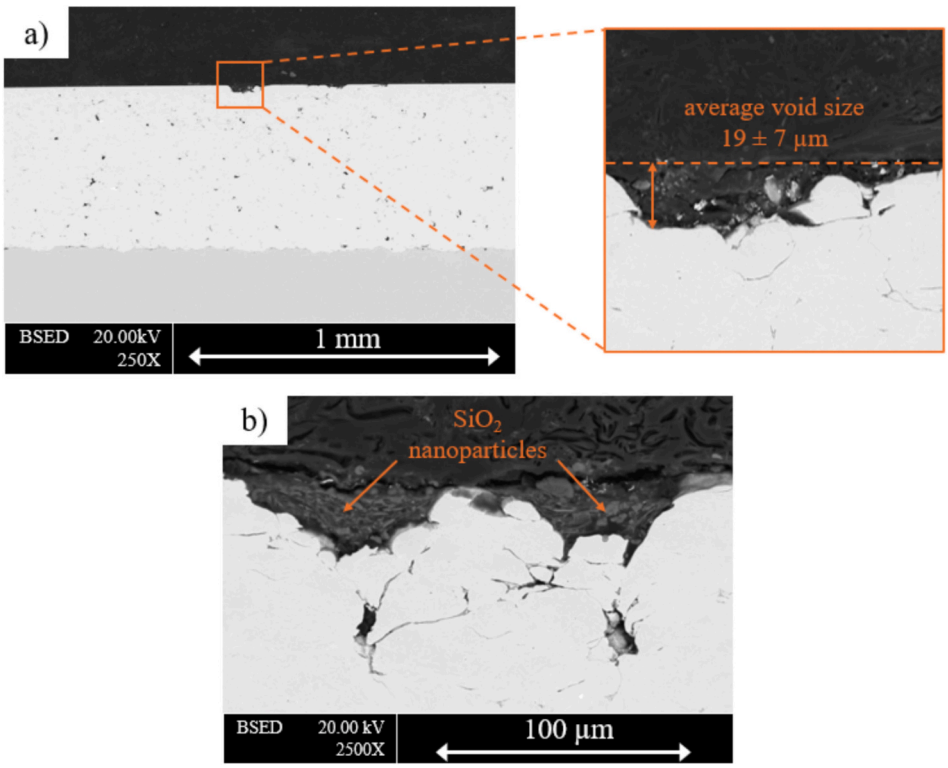

Fig. 5. SEM images of Inconel-625 CGS sample surface of a) voids formed and b) SiO_2 nanoparticle aggregation within the voids.

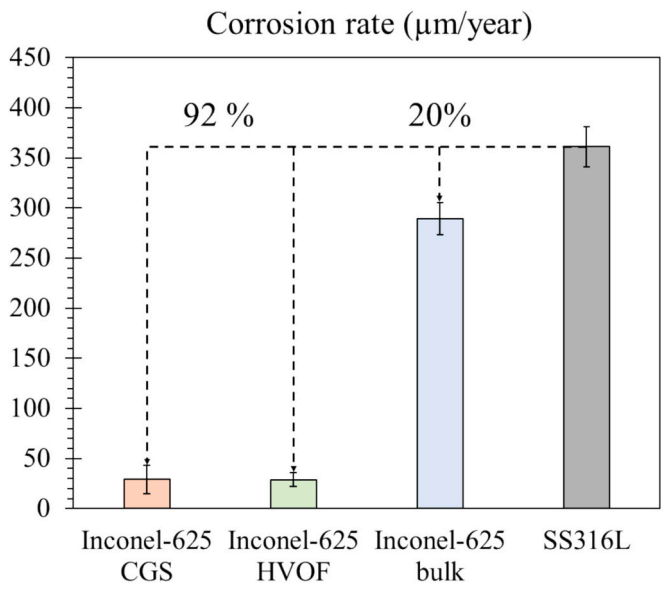

Fig. 6. Corrosion rate after 3 months in molten salt based nanofluids for: Inconel-625 HVOF (red bar), Inconel-625 CGS (green bar), Inconel-625 bulk (blue bar) and SS316L (grey bar).

during the test time (Table 2). For the Inconel-625 CGS samples, the first month (Fig. 3-a), no loss of coating thickness was observed. However, after 90 days of testing (Fig. 3-b), a minimal thickness loss of 7.2 ± 3 µm appeared, due to the formation of small holes that will be studied below. However, this variation is still within the measurement error. In the case of Inconel-625 deposited by HVOF, no loss of coating thickness was observed during the test (Fig. 3-c-d). The initial coating thickness is a key factor in this corrosion resistance, as a thick coating provides a greater barrier that prevents corrosion from reaching the substrate. However, excessive thickness can cause internal stresses that lead to cracks and loss of adhesion [42]. Generally, HVOF coatings are usually around 100–300 µm, while CGS coatings are thicker, reaching over 500 µm [43,44]. In this study, coatings of similar thickness were used to obtain a better comparison, taking into account that this thickness did not compromise morphology and performance.

Although no considerable reduction in coating thickness was observed, oxide layers appeared on the surface of all the samples, Fig. 4. This occurs to a higher degree in the samples exposed to molten salts for 3 months at 450 °C. On the one hand, for the Inconel-625 CGS samples (Fig. 4-a), this layer consisted predominantly of SiO_2 aggregates and some oxides in minor proportion due to material corrosion. These aggregations made layers with an average thickness of 13.1 ± 4 µm. On the other hand, for the Inconel-625 HVOF samples (Fig. 4-b), an oxide layer also appears on the surface after 90 days. This layer reaches an average of 8 ± 4 µm, which is smaller than that formed on the CGS samples.

If these results are compared with the uncoated substrate samples, it can be seen that the oxide layer formed is much larger (Fig. 4-c), with an average thickness of 89 ± 5 µm. These results can also be compared with Inconel-625 in bulk. Some studies have shown that the thermal projection of this material decreases its resistance to corrosion [45]. This is due to increased porosity, which allows corrosion advancement through the cracks or pores, and Cr content depletion. Regarding this, corrosion tests in which the Inconel-625 behaviour in solar salt has been studied showed corrosion rates of 0.146 × 10^{-2} µm/h in the first four days at 565 °C [46]. This was due to the corrosion layer formation of 100.98 µm depth for this test time. Similarly, in another study on the same salt but at 500 °C for 500 h, the appearance of small corrosion particles of 100–200 nm was observed [47]. However, for a more accurate comparison, the bulk Inconel-625 was tested under the same conditions as the coated samples (Fig. 4-d). In this case, the oxide layer formed on the surface was 71.4 ± 4 µm. Therefore, for this test conditions, the corrosion performance of thermally sprayed Inconel-625 samples was better than that of bulk Inconel-625. This would imply that by optimising the deposition parameters, adequately dense and well bonded coatings with excellent corrosion resistance can be achieved.

Furthermore, small voids caused by corrosion of the CGS coating surface also appeared (Fig. 5-a). This event was originated due to the coating deposited by CGS are less compact, since they are produced by plastic deformation of the particles impacting against the substrate. This allows corrosion advancement through the interconnected porosity [48]. However, the thickness of the coating prevents this progression from reaching the substrate. In addition, the nanoparticles tended to aggregate, filling these formed voids (Fig. 5-b).

From these results, it was possible to calculate the corrosion rate after 3 months of testing for each material (Fig. 6), following the procedure described above. For the 316 L stainless steel substrate material, a corrosion rate of 361.1 ± 20 µm/year (grey bar) was obtained after 90 days. Whereas, for bulk Inconel-625, this velocity was reduced by 20 %, reaching 289.5 ± 16 µm/year (blue bar). Finally, for coated samples, 29.1 ± 14 and 29 ± 7 µm/year values were obtained for CGS and HVOF, respectively. This resulted in a 92 % corrosion rate reduction compared with the substrate material.

Moreover, mappings of the cross sections of the HVOF and CGS samples were performed after 90 days of testing (Fig. 7). This allowed to corroborate the composition of the oxide layers formed. For the CGS sample (Fig. 7-a), the clear aggregation of SiO_2 nanoparticles in the formed voids was observed, as well as the advancement of the oxide through the interparticle cracks. Likewise, the formation of Ni, Cr, Nb and Mo oxides, base elements of Inconel-625, was also observed. This is consistent with other studies of this material's behaviour in corrosive environments [49,50]. In addition, Fe accumulation was observed on the surface of the hole areas. Thus, the presence of iron oxides on the surface of the sample causes the corrosion resistance of the coating to be attenuated [51]. In the case of HVOF (Fig. 7-b), the oxide layer formed was mostly composed of Ni, Cr, Nb and Mo oxides. The reason for this is that the reactions between sodium nitrate and these metals occur spontaneously at temperatures between 600 and 1000 K, forming different oxides of these metals [52]. Isolated iron particles also formed, due to the concentration of this element in some areas of the coating, which allowed the formation of iron oxides. In addition, the mapping allowed for observing the oxide layers formed due to the very high temperatures of the nozzle when the powder was deposited [53]. Finally, for this sample, almost no nanoparticle aggregation was observed on the surface.

These results for both samples are as expected for this material in contact with molten salts. In this sense, corrosion starts with the oxidation of Cr on the surface of the coating in contact with the molten salts [54]. Therefore, for the HVOF sample, having a lower Cr content in the coating, due to the chromium oxide layers already formed, oxidation occurs to a smaller degree. This oxidation would result in the diffusion of Cr atoms through the interparticle and oxidized zones, leading to precipitation of Ni, Nb and Mo [46,54]. However, during thermal cycling, studies indicate that this diffusion is reduced [46]. Producing a dense protective oxide layer on the surface through interstitial cooling.

Likewise, in order to have a better comparison, mappings of the SS316L (Fig. 7-c) and Inconel-625 bulk (Fig. 7-d) samples were carried out. The predominant presence of iron in the stainless-steel stands out, which agrees with the results of other studies carried out on solar salt [55]. The presence of Cr was also notable, as well as Si from small nanoparticle aggregations. For the bulk Inconel-625, something similar to the thermally sprayed Inconel-625 occurred. The mapping revealed a higher presence of Ni and Cr, as well as small accumulations of Si.

To explain the corrosion mechanisms that follow the samples under study, Fig. 8 shows the samples as spayed by CGS and HVOF (after a one-month test). The surface oxidation in the Inconel splats after a month of testing for the as-sprayed CGS and HVOF samples can be seen in free

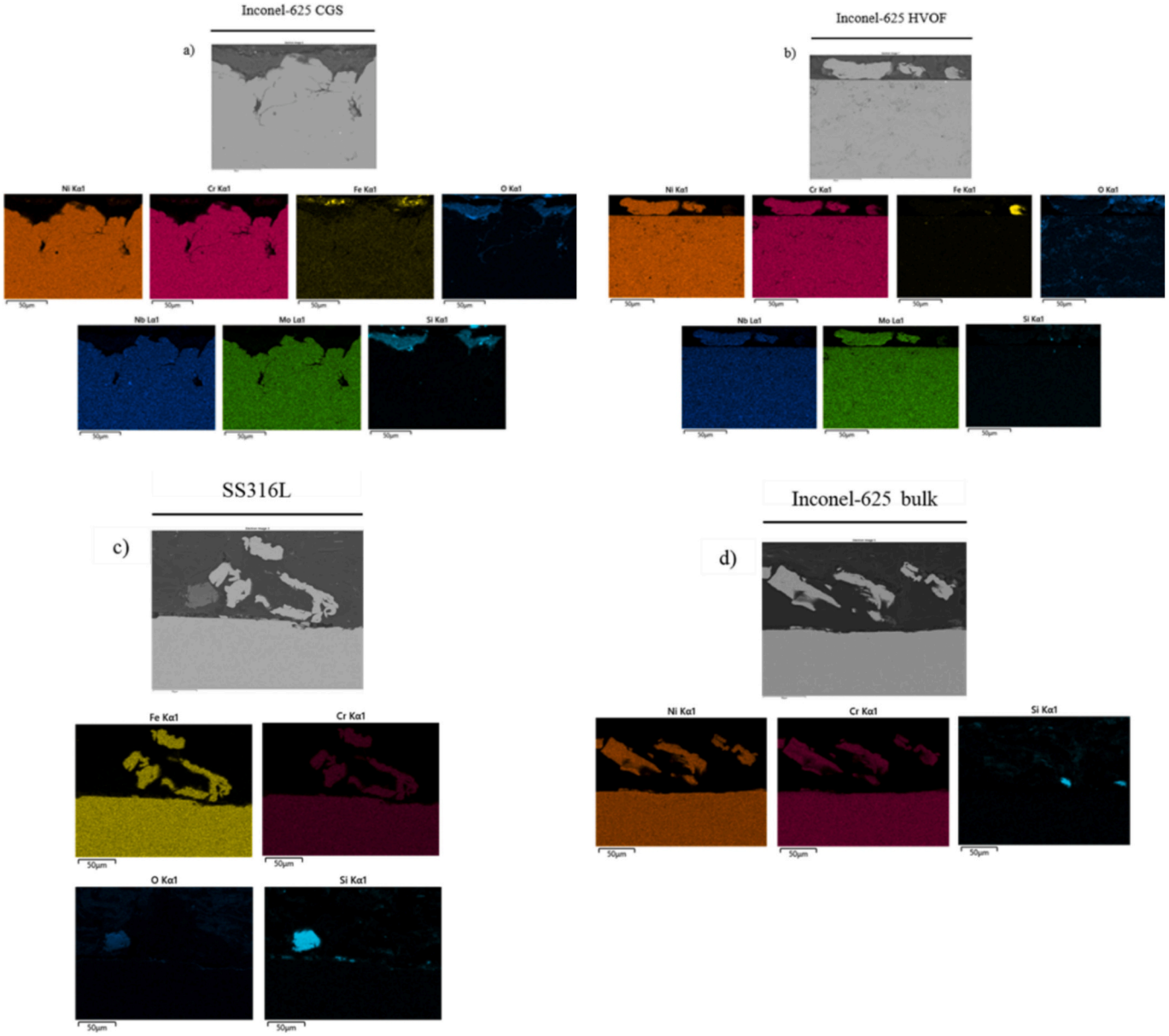

Fig. 7. EDS Mapping of the cross section of a) Inconel-625 CGS, b) Inconel-625 HVOF, c) SS316L and d) Inconel-625 bulk samples after 3 months of immersion in molten salt-based nanofluids.

surface FESEM micrographs shown in Fig. 8. In the case of the HVOF coating, the spreading of the molten particles' contrasts with the solid-state deposited by CGS (upper images). At high magnification, it is depicted how the corrosion front progresses through the intersplat zones in the particles with less cohesion, or even through the porosity between particles. This fact explains the mechanism of corrosion for these materials, going through the intersplat boundaries and detaching outer particles after 3 months (~30 μm). Fig. 8 also shows the EDX mappings for both HVOF and CGS coating surfaces (right images), showing the existence of O, Na, and Si coming from the nanofluids and the oxidation of the particles.

To better understand the corrosive behaviour of the nanofluids, the free surface of Inconel-625 HVOF and CGS, SS316L, and Inconel-625 bulk samples (30 and 90 days) were examined (Fig. 9). Regarding the CGS samples, these were more affected by corrosion in comparison to HVOF samples. For the first month of testing, the formation of micro-holes was observed on a large part of the sample surface (Fig. 9-a). This could have been caused by interparticle porosity due to plastic deformation of the powder particles, as discussed above. However, the previous roughing of the surface of the samples could reduce this effect, thus decreasing the number of holes and fractures originated. The amount of surface damage increases as the test time increases. Thus, after 90 days, the size of the holes is much larger. Additionally, it was observed that the nanoparticles accumulated inside these voids and cracks (Fig. 9-b). However, on the other hand, for the HVOF samples, the corrosion effect caused by the nanofluids was almost imperceptible. After the first 30 days, the sample could be seen with no signs of damage at the surface level (Fig. 9-c). Only small aggregations of nanoparticles with diameters of <20 μm appeared. While after 3 months in the furnace, these agglomerations grew considerably (Fig. 9-d). For this period of time no damage was observed on the sample, which demonstrated the effectiveness of the Inconel-625 coating deposited by HVOF. Comparing both coated samples with the substrate (Fig. 9-e and Fig. 9-f), the positive and anticorrosive effect of the thermally sprayed Inconel-625 coatings was verified. The degradation of the stainless-steel base material was much higher, with numerous surface cracks and a large

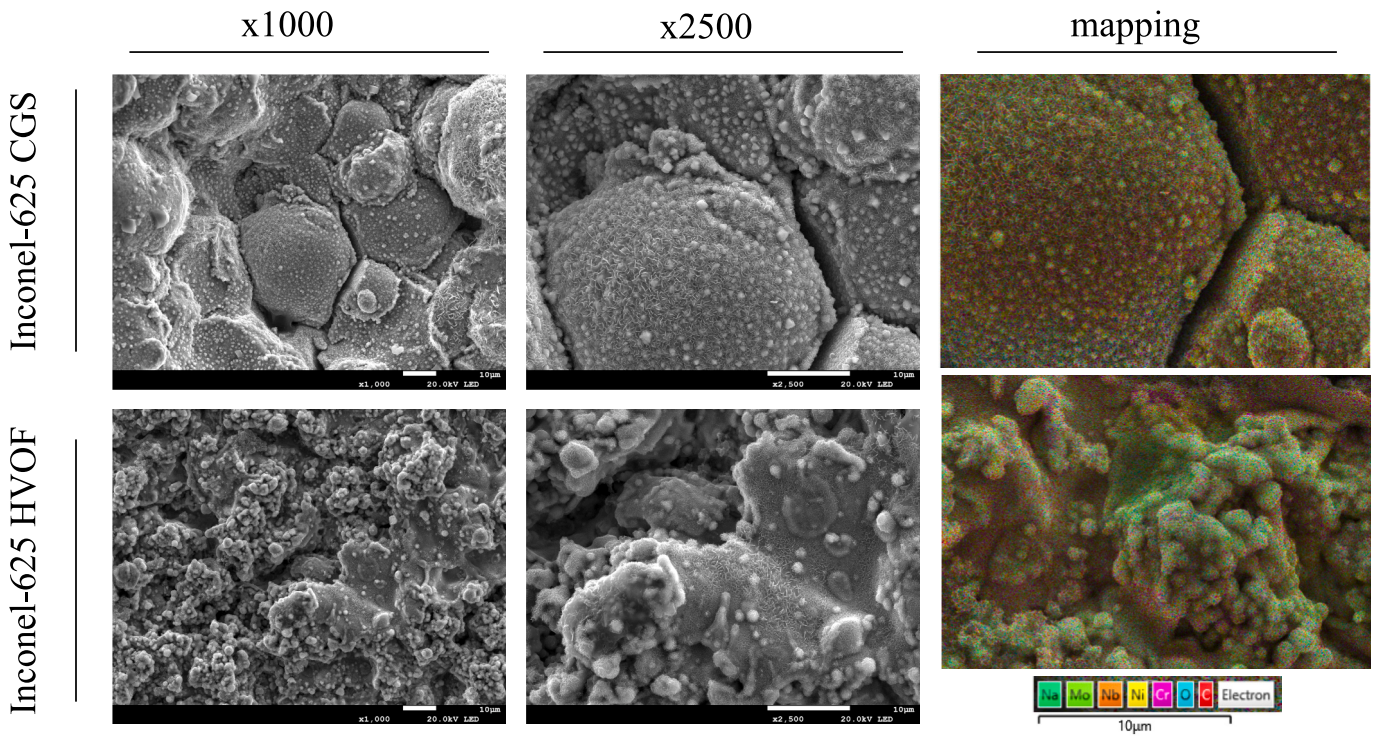

Fig. 8. As-sprayed SEM images of the samples by CGS (up), and HVOF (down), and content mapping considering Na, Mo, Nb, Ni, Cr, O, and C content (right).

agglomeration of nanoparticles around them. Finally, the results for bulk Inconel-625 (Fig. 9-g and Fig. 9-h) showed a similar tendency as mentioned above. Small aggregations of SiO_2 were observed on the surface, increasing with longer exposure time. In addition, surface degradation due to corrosion could be noted, becoming rougher and cracked. However, this surface modification was less pronounced than for the stainless-steel substrate.

In addition, there are different studies that support that the addition of nanoparticles to molten salts reduces the corrosive behaviour of these salts and, therefore, the oxide layers formed [56,57]. This is mainly due to the incorporation of these nanoparticles into the oxide layers, as is the case with the CGS samples in this study. Moreover, these investigations also reflect the tendency of the nanoparticles to aggregate with increasing test time. However, there are other studies indicating that the presence of nanoparticles can increase the corrosion rate of different alloys [58]. Although, in the case of Inconel-type superalloys, this effect is less pronounced. The effects of the addition of nanoparticles on the corrosion behaviour of molten salts is a field for further research. Even so, it has been demonstrated that they have a notable influence depending on the test conditions and materials tested.

XRD analysis of the samples was carried out to study aspects observed in the free surface micrographs. For a better comparison, the powders used and the coatings before and after the test were analysed (Fig. 9). Thus, it was possible to evaluate potential phase changes in the coating deposition and surface oxides formed on the coating surface. On the one hand, in the case of both powders (black lines) and coatings (blue lines), the main crystallographic phase corresponds γ matrix (Ni, Cr, Fe alloy) with a cubic structure, typical of Inconel-625 [59,60]. Additionally, a minor phase of Cr_2O_3 oxide was identified in both samples. However, small peak modifications can be observed due to the deposition technique. In the case of the HVOF sample (Fig. 9-a, blue line), narrower peaks were observed, whereas for the CGS (Fig. 9-b, blue line), these were broader and less well-defined. The main reason is that this technique forms coatings with more defects due to the particles' plastic micro-deformation on impact with the substrate [61]. Moreover, the peaks widening indicates a smaller crystallite size formation through the CGS technique.

Coatings after a 3-month corrosion test (Fig. 10-a, b, grey lines) show small structural modifications. The peak intensity of the main Inconel-625 phase significantly weakened. In contrast, NiO and Cr_2O_3 minor phases appear, increasing the thickness of the oxidized layer and indicating the oxidation of the coating surface during the corrosion at 450 °C, as seen in Figs. 4–6. On the contrary, the diffraction peaks of the Cr_2O_3 formed during the deposition disappear after the test, indicating its release to the molten salts. The peak intensity of the formed oxides on the surface of the coatings is more pronounced in the CGS samples, implying higher oxide content on the coating surface. Minor elements like Mo or Nb, detected in the EDS mapping of Fig. 6, cannot be detected by the limit detection. Additionally, SiO_2 peaks appear in the two samples, where the peak intensity is more pronounced in the CGS samples, as seen in Fig. 7. The presence of SiO_2 on the coating's surface can reduce the corrosion rates due to the incorporation of the nanoparticles into the oxide layer, as indicates the study performed by Nithiyanantham et al. [56].

Regarding the metal analysis (ICP) results (see Fig. 11), metals corresponding to Inconel-625 were found in both samples. In the salt in contact with the Inconel-625 CGS sample, 4.4 ± 0.3 μg/g Ni and 12 ± 2 μg/g Cr were detected in its composition. In contrast, for the Inconel-625 HVOF sample, amounts of 2.07 ± 0.10 μg/g Ni, 219 ± 13 μg/g Cr, and 48.4 ± 2.7 μg/g Mo were detected. This mainly indicates the release of Ni and Cr to the molten salts during the corrosion test, which is in accordance with the literature [62,63]. Finally, the Si content of the molten salt-based nanofluids was not significant.

In the case of the HVOF sample, oxidation reactions occur due to the high temperatures of the nozzle when the powders are sprayed, the particles' exposure to the flame's atmosphere and the particles' exposure to the environment once they have been deposited [45,53]. This promotes the formation of Cr_2O_3 lamellae throughout the coating (Fig. 11-a) which act as protective barriers that reduce the progress of corrosion [64,65]. This passive layer acts as a barrier, preventing oxygen, and other corrosive agents from reaching the underlying material. However, the oxide layers were less clear after the corrosion test (Fig. 11-b), which

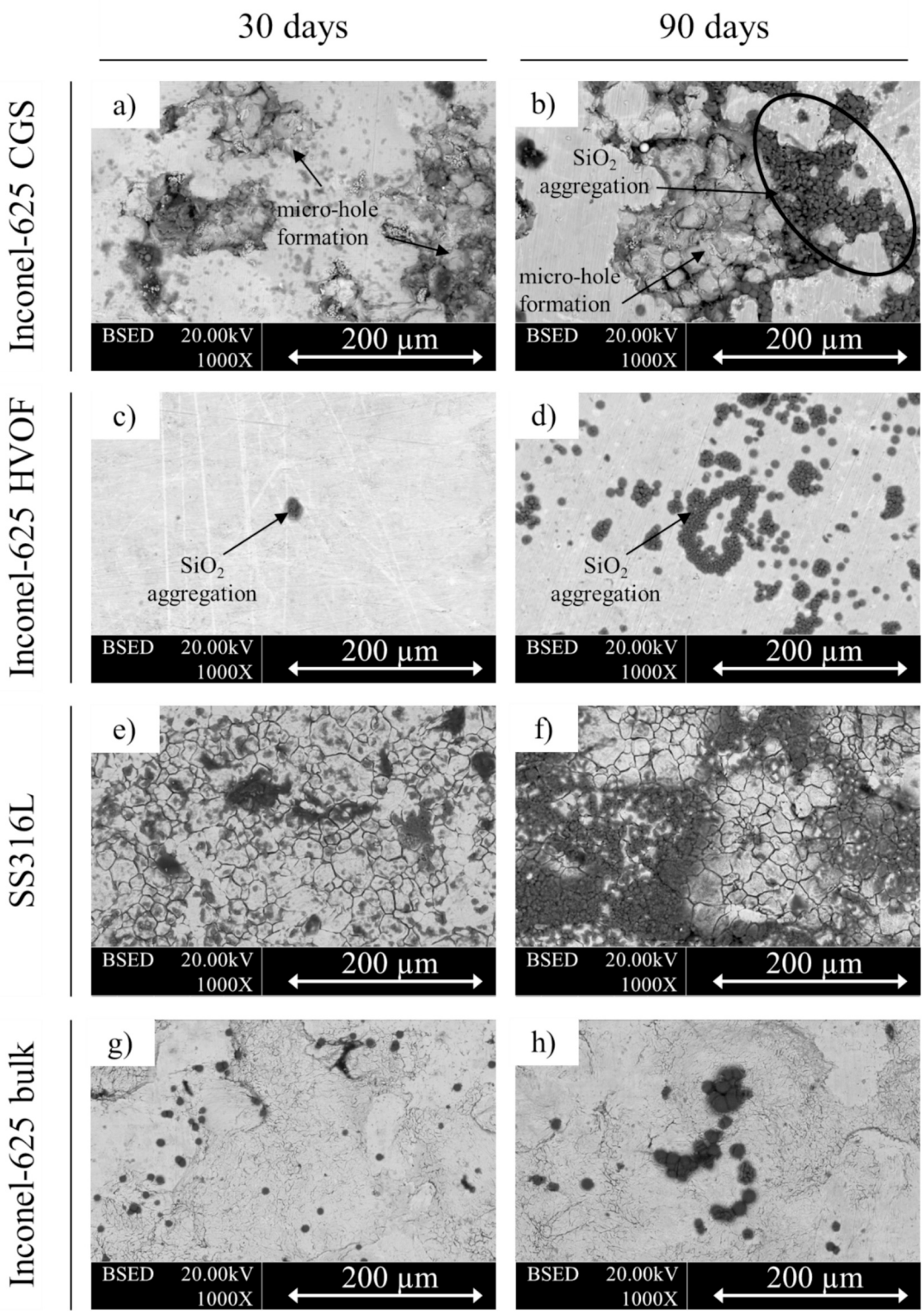

Fig. 9. Free surface of the samples of a) Inconel-625 CGS after 1 month, b) Inconel-625 CGS after 3 months, c) Inconel-625 HVOF after 1 month, d) Inconel-625 HVOF after 3 months, e) SS316L after 1 month, f) SS316L after 3 months, g) Inconel-625 bulk after 1 month, and h) Inconel-625 bulk after 3 months.

is consistent with the disappearance of the Cr_2O_3 diffraction peaks. This reduction could have been due to two main reasons: transformation into other phases or the diffusion of Cr into the molten salt [62,63]. The transformation of Cr_2O_3 into other phases could result in chromates (e.g. Na_2CrO_4, $NiCr_2O_4$, $FeCr_2O_4$) or mixed oxides due to the presence of $NaNO_3$, which increases susceptibility to corrosion. On the other hand, these oxide layers cause a Cr depletion in the surrounding regions, which results in a concentration gradient. Therefore, Cr could diffuse towards the surface more easily [66], which explains the increased Cr content found in the ICP analysis.

4. Conclusions

The results obtained confirmed the excellent performance of thermal

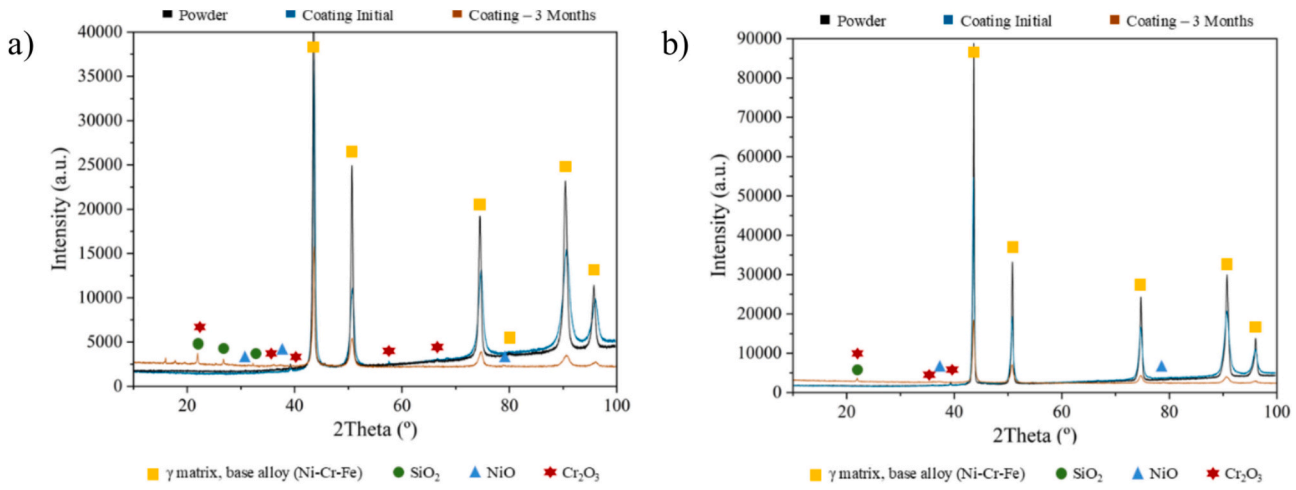

Fig. 10. XRD patterns of a) HVOF Inconel-625: Powder (black line), Initial coating (blue line) and coating after 3 months corrosion test at 450 °C (orange line) and, b) CGS Inconel-625: Powder (black line), Initial coating (blue line) and coating after 3 months corrosion test at 450 °C (orange line).

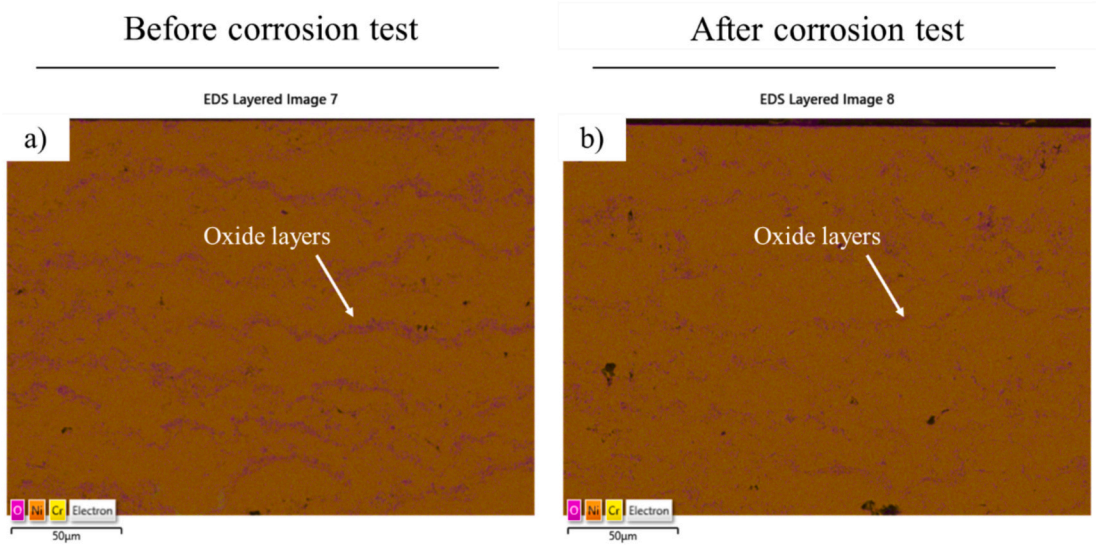

Fig. 11. Mapping of the HVOF coating: a) before the test and b) after the test.

spray coatings against corrosion caused by molten salt-based nanofluids (molten $NaNO_3$ with SiO_2 nanoparticles). The main conclusions derived from this work are presented below:

- Although the formation of oxide layers was observed for both coatings, the loss of thickness was minimal. Values of 13.1 ± 4 μm for Inconel-625 CGS and 8 ± 4 μm for Inconel-625 HVOF were reached. Thus, the corrosion rate was reduced by 92 % compared to the 316 L stainless steel substrate and by 90 % compared to bulk Inconel-625. However, this test should be performed under thermal cycling conditions to confirm that better results are also obtained for thermally sprayed Inconel-625. As these conditions are closer to the actual operating conditions of CSP plants.
- In the CGS samples, small holes were observed on the coating surface. This was mainly due to the coating deposition nature, which by plastic deformation of the particles, produces a less compact layer. Nevertheless, previous roughing of the surface of the samples could reduce this effect.
- Surface analysis and mappings revealed the aggregation of SiO_2 nanoparticles on the sample surface This behaviour could act as a protective barrier, thus reducing the corrosion rate. However, further investigation of this phenomenon and its effects on the samples is required.
- Metal analysis showed a clear diffusion of Inconel-625 elements (Cr, Ni and Mo) into the molten salt. This could lead to a change in the salt's thermal properties and would need to be tested to evaluate this.

CRediT authorship contribution statement

Lorena Betancor-Cazorla: Writing – original draft, Validation, Methodology, Investigation, Data curation. **Adela Svobodova-Sedlackova:** Software, Investigation, Formal analysis, Data curation. **Genís Clavé:** Investigation, Data curation. **Camila Barreneche:** Writing – review & editing, Supervision, Methodology, Investigation, Formal analysis, Data curation. **Sergi Dosta:** Writing – review & editing, Validation, Supervision, Resources, Project administration, Methodology, Investigation, Funding acquisition, Formal analysis, Data curation, Conceptualization.

Declaration of competing interest

The authors declare that they have no known competing financial

interests or personal relationships that could have appeared to influence the work reported in this paper.

Acknowledgments

The authors would like to thank the Catalan Government for the quality accreditation given to their research group DIOPMA (2021 SGR 00708 and 2021 SGR 00512). DIOPMA is a certified agent TECNIO in the category of technology developers from the Government of Catalonia. This work has been partially funded by the Spanish government PID2021-123511OB-C32 (MICINN/FEDER, UE) and supported by "100 Foreign Experts Plan of Hebei Province". This work couldn't be carried out without the support of "Thermodust" project (n. 101046835) funded by the "Horizon Europe" framework programme, and also CDTI and NextGeneration EU funds for the Bioenergy project MIP-20221004. Additionally, special thanks to TM COMAS SLU company and Titomic Europe B.V, which supported the project by providing the coating samples for testing.

Data availability

Data will be made available on request.

References

[1] International Energy Agency, Renewables 2023. Analysis and forecast to 2028, International Energy Agency IEA (Jan. 2024) [Online]. Available: www.iea.org.
[2] S.J. Wagner, E.S. Rubin, Economic implications of thermal energy storage for concentrated solar thermal power, Renew. Energy 61 (Jan. 2014) 81–95, https://doi.org/10.1016/j.renene.2012.08.013.
[3] O. Achkari, A. El Fadar, Latest developments on TES and CSP technologies – energy and environmental issues, applications and research trends, Appl. Therm. Eng. 167 (Feb. 2020) 114806, https://doi.org/10.1016/j.applthermaleng.2019.114806.
[4] REN21, 'Renewables 2023 Global Status Report Collection, Global Overview', REN21. [Online]. Available: https://www.ren21.net/gsr-2023/modules/global_overview/.
[5] International Renewable Energy Agency IRENA, World energy transitions. Outlook 2023 : 1.5°C pathway, 2023.
[6] G. Peiró, C. Prieto, J. Gasia, A. Jové, L. Miró, L.F. Cabeza, Two-tank molten salts thermal energy storage system for solar power plants at pilot plant scale: lessons learnt and recommendations for its design, start-up and operation, Renew. Energy 121 (2018) 236–248, https://doi.org/10.1016/j.renene.2018.01.026.
[7] C. Prieto, R. Osuna, A.I. Fernández, L.F. Cabeza, Thermal storage in a MW scale. Molten salt solar thermal pilot facility: plant description and commissioning experiences, Renew. Energy 99 (Dec. 2016) 852–866, https://doi.org/10.1016/j.renene.2016.07.053.
[8] M. Mubarrat, M.M. Mashfy, T. Farhan, M.M. Ehsan, Research advancement and potential prospects of thermal energy storage in concentrated solar power application, Int. J. Thermofluids 20 (Nov. 2023) 100431, https://doi.org/10.1016/j.ijft.2023.100431.
[9] Sandia National Laboratories, Final test and evaluation results from the Solar Two project, 2002.
[10] T. Bauer, N. Pfleger, D. Laing, W.-D. Steinmann, M. Eck, S. Kaesche, 20- high-temperature molten salts for solar power application, in: F. Lantelme, H. Groult (Eds.), Molten salts chemistry, Elsevier, Oxford, 2013, pp. 415–438, https://doi.org/10.1016/B978-0-12-398538-5.00020-2.
[11] C. Prieto, A. Blindu, L.F. Cabeza, J. Valverde, G. García, Molten salts tanks thermal energy storage: aspects to consider during design, Energies 17 (1) (Dec. 2023) 22, https://doi.org/10.3390/en17010022.
[12] M. Sarvghad, T.A. Steinberg, G. Will, Corrosion of stainless steel 316 in eutectic molten salts for thermal energy storage, Sol. Energy 172 (Sep. 2018) 198–203, https://doi.org/10.1016/j.solener.2018.03.053.
[13] N. Ko, M. Lorenz, R. Horn, H. Krieg, M. Baumann, Sustainability assessment of concentrated solar power (CSP) tower plants–integrating LCA, LCC and LCWE in one framework, Procedia CIRP 69 (2018) 395–400, https://doi.org/10.1016/j.procir.2017.11.049.
[14] C. Prieto, R. Osuna, A.I. Fernández, L.F. Cabeza, Molten salt facilities, lessons learnt at pilot plant scale to guarantee commercial plants; heat losses evaluation and correction, Renew. Energy 94 (Aug. 2016) 175–185, https://doi.org/10.1016/j.renene.2016.03.039.
[15] A.H. Pordanjani, et al., Nanofluids: physical phenomena, applications in thermal systems and the environment effects- a critical review, J. Clean. Prod. 320 (Oct. 2021) 128573, https://doi.org/10.1016/j.jclepro.2021.128573.
[16] R. Serrano-López, J. Fradera, S. Cuesta-López, Molten salts database for energy applications, Chem. Eng. Process. Process Intensif. 73 (Nov. 2013) 87–102, https://doi.org/10.1016/j.cep.2013.07.008.
[17] A. Svobodova-Sedlackova, et al., Using statistical analysis to create a new database of Nanofluids' specific heat capacity, J. Mol. Liq. 369 (Jan. 2023) 120847, https://doi.org/10.1016/j.molliq.2022.120847.
[18] Q. Xiong, A. Hajjar, B. Alshuraiaan, M. Izadi, S. Altnji, S.A. Shehzad, State-of-the-art review of nanofluids in solar collectors: a review based on the type of the dispersed nanoparticles, J. Clean. Prod. 310 (Aug. 2021) 127528, https://doi.org/10.1016/j.jclepro.2021.127528.
[19] A. Svobodova, A. Calderon, C. Barreneche, P. Gamallo, A. Fernández, Understanding the abnormal thermal behavior of nanofluids through infrared thermography and thermo-physical characterization, Sci. Rep. 11 (Mar. 2021), https://doi.org/10.1038/s41598-021-84292-9.
[20] S.M.M. Rizvi, D. Shin, Mechanism of heat capacity enhancement in molten salt nanofluids, Int. J. Heat Mass Transf. 161 (Nov. 2020) 120260, https://doi.org/10.1016/j.ijheatmasstransfer.2020.120260.
[21] S.M.M. Rizvi, D. Shin, Specific heat capacity, viscosity, and thermal stability of carbonate-based molten salt nanofluids, J. Energy Storage 43 (Nov. 2021) 103192, https://doi.org/10.1016/j.est.2021.103192.
[22] A.G.N. Sofiah, M. Samykano, A.K. Pandey, K. Kadirgama, K. Sharma, R. Saidur, Immense impact from small particles: review on stability and thermophysical properties of nanofluids, Sustain Energy Technol Assess 48 (Dec. 2021) 101635, https://doi.org/10.1016/j.seta.2021.101635.
[23] P. Gimenez, S. Fereres, Effect of heating rates and composition on the thermal decomposition of nitrate based molten salts, Energy Procedia 69 (May 2015) 654–662, https://doi.org/10.1016/j.egypro.2015.03.075.
[24] A. Svobodova-Sedlackova, S. Huete-Hernández, A. Calderón, C. Barreneche, P. Gamallo, A.I. Fernandez, Effect of nanoparticles on the thermal stability and reaction kinetics in ionic nanofluids, Nanomaterials 12 (10) (2022), https://doi.org/10.3390/nano12101777.
[25] M. Vaka, R. Walvekar, M. Khalid, P. Jagadish, J.H. Low, Corrosion, rheology, and thermal ageing behaviour of the eutectic salt-based graphene hybrid nanofluid for high-temperature TES applications, J. Mol. Liq. 334 (Jul. 2021) 116156, https://doi.org/10.1016/j.molliq.2021.116156.
[26] U. Nithiyanantham, Y. Grosu, L. González-Fernández, A. Zaki, J.M. Igartua, A. Faik, Development of molten nitrate salt based nanofluids for thermal energy storage application: high thermal performance and long storage components life-time, AIP Conf. Proc. 2126 (1) (Jul. 2019) 200025, https://doi.org/10.1063/1.5117740.
[27] U. Nithiyanantham, et al., Nanoparticles as a high-temperature anticorrosion additive to molten nitrate salts for concentrated solar power, Sol. Energy Mater. Sol. Cells 203 (Dec. 2019) 110171, https://doi.org/10.1016/j.solmat.2019.110171.
[28] L. Ma, C. Zhang, Y. Wu, Y. Lu, Comparative review of different influence factors on molten salt corrosion characteristics for thermal energy storage, Sol. Energy Mater. Sol. Cells 235 (Jan. 2022) 111485, https://doi.org/10.1016/j.solmat.2021.111485.
[29] S. Dosta, L. Betancor, C. Barreneche, Overview of surface engineering technology to improve the energy efficiency in concentrated solar power (CSP) plants, Sol. Energy Mater. Sol. Cells 277 (Oct. 2024) 113090, https://doi.org/10.1016/j.solmat.2024.113090.
[30] A.S. Dinkar, H. Panchal, A review on thermal spray coating processes 2 (4) (2016).
[31] N. Li, et al., Corrosion-resistant thermal spray coatings for low-alloy steel in contact with molten nitrate salts in solar power plants, Sol. Energy Mater. Sol. Cells 259 (Aug. 2023) 112432, https://doi.org/10.1016/j.solmat.2023.112432.
[32] D. Guo, et al., Cold spray: over 30 years of development toward a hot future, J. Therm. Spray Technol. 31 (4) (Apr. 2022) 866–907, https://doi.org/10.1007/s11666-022-01366-4.
[33] D. Fantozzi, V. Matikainen, M. Uusitalo, H. Koivuluoto, P. Vuoristo, Chlorine-induced high temperature corrosion of Inconel 625 sprayed coatings deposited with different thermal spray techniques, Surf. Coat. Technol. 318 (May 2017) 233–243, https://doi.org/10.1016/j.surfcoat.2016.12.086.
[34] J. Karthikeyan, 4- The advantages and disadvantages of the cold spray coating process, in: V.K. Champagne (Ed.), The Cold Spray Materials Deposition Process, Woodhead Publishing Series in Metals and Surface Engineering, Woodhead Publishing, 2007, pp. 62–71, https://doi.org/10.1533/9781845693787.1.62.
[35] J.E. Berger, et al., Wear and corrosion properties of HVOF coatings from Superduplex alloy modified with addition of boron, Surf. Coat. Technol. 309 (Jan. 2017) 911–919, https://doi.org/10.1016/j.surfcoat.2016.10.062.
[36] J.C. Gomez-Vidal, J. Noel, J. Weber, Corrosion evaluation of alloys and MCrAlX coatings in molten carbonates for thermal solar applications, Sol. Energy Mater. Sol. Cells 157 (Dec. 2016) 517–525, https://doi.org/10.1016/j.solmat.2016.07.029.
[37] J. Luo, et al., Robust corrosion performance of cold sprayed aluminide coating in ternary molten carbonate salt for concentrated solar power plants, Sol. Energy Mater. Sol. Cells 237 (Apr. 2022) 111573, https://doi.org/10.1016/j.solmat.2021.111573.
[38] C. Senderowski, N. Cinca, S. Dosta, I.G. Cano, J.M. Guilemany, The effect of hot treatment on composition and microstructure of HVOF iron aluminide coatings in Na2SO4 molten salts, J. Therm. Spray Technol. 28 (7) (Oct. 2019) 1492–1510, https://doi.org/10.1007/s11666-019-00886-w.
[39] F. Rubino, P. Poza, G. Pasquino, P. Carlone, Thermal spray processes in concentrating solar power technology, Metals 11 (Aug. 2021) 1377, https://doi.org/10.3390/met11091377.
[40] A. Svobodova-Sedlackova, C. Barreneche, P. Gamallo, A.I. Fernández, Novel sampling procedure and statistical analysis for the thermal characterization of ionic nanofluids, J. Mol. Liq. 347 (Feb. 2022) 118316, https://doi.org/10.1016/j.molliq.2021.118316.

[41] C09 Committee, Practice for Reducing Samples of Aggregate to Testing Size. doi: https://doi.org/10.1520/C0702_C0702M-11.
[42] V. Lakkannavar, K.B. Yogesha, C.D. Prasad, R.K. Phanden, S. G, S.C. Prasad, Thermal spray coatings on high-temperature oxidation and corrosion applications – a comprehensive review, Results Surf. Interfaces 16 (2024) 100250, https://doi.org/10.1016/j.rsurfi.2024.100250.
[43] S. Singh, K. Goyal, R. Bhatia, Mechanical and microstructural properties of yttria-stabilized zirconia reinforced Cr3C2-25NiCr thermal spray coatings on steel alloy: original scientific paper, J. Electrochem. Sci. Eng. 12 (5) (2022) 5, https://doi.org/10.5599/jese.1278.
[44] A. Silvello, P. Cavaliere, S. Yin, R. Lupoi, I. Garcia Cano, S. Dosta, Microstructural, mechanical and wear behavior of HVOF and cold-sprayed high-entropy alloys (HEAs) coatings, J. Therm. Spray Technol. 31 (4) (Apr. 2022) 1184–1206, https://doi.org/10.1007/s11666-021-01293-w.
[45] N. Ahmed, M.S. Bakare, D.G. McCartney, K.T. Voisey, The effects of microstructural features on the performance gap in corrosion resistance between bulk and HVOF sprayed Inconel 625, Surf. Coat. Technol. 204 (14) (Apr. 2010) 2294–2301, https://doi.org/10.1016/j.surfcoat.2009.12.028.
[46] Y. Su, H. Li, T. Yang, Z. Dai, G. Zhang, Study on the corrosion behavior of inconel 625 deposited metal against molten nitrate, Mater. Today Commun. 40 (Aug. 2024) 109699, https://doi.org/10.1016/j.mtcomm.2024.109699.
[47] C. Liu, et al., The characterization of corrosion layers of GH3535 and Inconel 625 alloys in molten KNO3-NaNO3 salts at 500 °C, Corros. Sci. 204 (Aug. 2022) 110406, https://doi.org/10.1016/j.corsci.2022.110406.
[48] F. Santos da Silva, N. Cinca, S. Dosta, I.G. Cano, A. Benedetti, J.M. Guilemany, Cold gas spray coatings: basic principles, corrosion protection and applications, Eclética Quím. J. 42 (Dec. 2017) 09, https://doi.org/10.26850/1678-4618eqj.v42.1.2017.p09-32.
[49] A. Soleimani Dorcheh, R.N. Durham, M.C. Galetz, Corrosion behavior of stainless and low-chromium steels and IN625 IN molten nitrate salts at 600 °C, Sol. Energy Mater. Sol. Cells 144 (Jan. 2016) 109–116, https://doi.org/10.1016/j.solmat.2015.08.011.
[50] M. Prem Kumar, M. Manikandan, Insights into the surface behavior of Inconel 617 and Inconel 625 material in molten salt, Mater. Lett. 333 (Feb. 2023) 133679, https://doi.org/10.1016/j.matlet.2022.133679.
[51] M. Solecka, Investigation of Ni-base coatings after corrosion test, Inż. Mater. 1 (Aug. 2016) 44–49, https://doi.org/10.15199/28.2016.4.7.
[52] C. Yang, X. Wei, Q. Peng, J. Ding, J. Yang, Effect of nickel base alloy on NO x emissions from binary molten nitrate salts in thermal energy storage process, Energy Procedia 105 (May 2017) 4003–4008, https://doi.org/10.1016/j.egypro.2017.03.837.
[53] M. Taghian, et al., High-velocity oxy-fuel (HVOF) spray coating of Inconel, Colmonoy, and aluminum on AISI 316L stainless steel: a comparative investigation of the microstructure and corrosion resistance of coatings, Coatings 13 (1) (2023), https://doi.org/10.3390/coatings13010204.
[54] H. Liu, et al., Hot corrosion and internal spallation of laser-cladded inconel 625 superalloy coatings in molten sulfate salts, Corros. Sci. 193 (Dec. 2021) 109869, https://doi.org/10.1016/j.corsci.2021.109869.
[55] A. Palacios, et al., High-temperature corrosion behaviour of metal alloys in commercial molten salts, Sol. Energy 201 (May 2020) 437–452, https://doi.org/10.1016/j.solener.2020.03.010.
[56] U. Nithiyanantham, Y. Grosu, L. González-Fernández, A. Zaki, J.M. Igartua, A. Faik, Corrosion aspects of molten nitrate salt-based nanofluids for thermal energy storage applications, Sol. Energy 189 (Sep. 2019) 219–227, https://doi.org/10.1016/j.solener.2019.07.050.
[57] L. Ma, C. Zhang, Y. Wu, Y. Lu, Effect of flow rate and SiO2 nanoparticle on dynamic corrosion behavior of stainless steels in molten salt for thermal energy storage, Corros. Sci. 194 (Jan. 2022) 109952, https://doi.org/10.1016/j.corsci.2021.109952.
[58] M.E. Navarro, et al., Effect of SiO2 nanoparticles concentration on the corrosion behaviour of solar salt-based nanofluids for concentrating solar power plants, Sol. Energy Mater. Sol. Cells 247 (Oct. 2022) 111923, https://doi.org/10.1016/j.solmat.2022.111923.
[59] K. Feng, et al., Improved high-temperature hardness and wear resistance of Inconel 625 coatings fabricated by laser cladding, J. Mater. Process. Technol. 243 (May 2017) 82–91, https://doi.org/10.1016/j.jmatprotec.2016.12.001.
[60] D. Zhang, S.J. Harris, D.G. McCartney, Microstructure formation and corrosion behaviour in HVOF-sprayed Inconel 625 coatings, Mater. Sci. Eng. A 344 (1–2) (Mar. 2003) 45–56, https://doi.org/10.1016/S0921-5093(02)00420-3.
[61] F. Taherkhani, A. List, S. Keller, N. Kashaev, F. Gärtner, T. Klassen, The influence of spraying parameters and powder sizes on the microstructure and mechanical behavior of cold-sprayed Inconel®625 deposits, J. Therm. Spray Technol. 33 (2) (Mar. 2024) 652–665, https://doi.org/10.1007/s11666-024-01712-8.
[62] G. McConohy, A. Kruizenga, Molten nitrate salts at 600 and 680 °C: Thermophysical property changes and corrosion of high-temperature nickel alloys, Sol. Energy 103 (May 2014) 242–252, https://doi.org/10.1016/j.solener.2014.01.028.
[63] M. Solecka, A. Radziszewska, B. Rutkowski, New insight on study of Ni-base alloy clad layer after oxidation at 650°C, Corros. Sci. 149 (Apr. 2019) 244–248, https://doi.org/10.1016/j.corsci.2019.01.013.
[64] J. Feng, et al., Probing layered structure of Inconel 625 coatings prepared by magnetron sputtering, Surf. Coat. Technol. 405 (Jan. 2021) 126545, https://doi.org/10.1016/j.surfcoat.2020.126545.
[65] K.-S. Lim, W.-S. Choi, W.-B. Kim, S.-H. Cho, J.-H. Lee, Effect of Cr content on hot corrosion behavior of Inconel alloys in molten LiCl–Li2O, High Temp. Corros. Mater. 100 (3) (2023) 345–358, https://doi.org/10.1007/s11085-023-10180-4.
[66] S. Yugeswaran, et al., Thermal conductivity and oxidation behavior of porous Inconel 625 coating interface prepared by dual-injection plasma spraying, Surf. Coat. Technol. 411 (Apr. 2021) 126990, https://doi.org/10.1016/j.surfcoat.2021.126990.